

# Scintillator detector characterization for laser-driven proton beam imaging

Cite as: Rev. Sci. Instrum. **91**, 123304 (2020); <https://doi.org/10.1063/5.0022166>

Submitted: 17 July 2020 • Accepted: 05 December 2020 • Published Online: 22 December 2020

 H. Tang,  B. K. Russell,  A. Maksimchuk, et al.



View Online



Export Citation



CrossMark

## ARTICLES YOU MAY BE INTERESTED IN

[Enhanced spatial resolution of Eljen-204 plastic scintillators for use in rep-rated proton diagnostics](#)

Review of Scientific Instruments **91**, 103301 (2020); <https://doi.org/10.1063/5.0014949>

[Target normal sheath acceleration with a large laser focal diameter](#)

Physics of Plasmas **27**, 123104 (2020); <https://doi.org/10.1063/5.0020609>

[Scaling of laser-driven electron and proton acceleration as a function of laser pulse duration, energy, and intensity in the multi-picosecond regime](#)

Physics of Plasmas **28**, 013108 (2021); <https://doi.org/10.1063/5.0023612>

Lock-in Amplifiers  
up to 600 MHz



Zurich  
Instruments



# Scintillator detector characterization for laser-driven proton beam imaging

Cite as: *Rev. Sci. Instrum.* **91**, 123304 (2020); doi: [10.1063/5.0022166](https://doi.org/10.1063/5.0022166)

Submitted: 17 July 2020 • Accepted: 5 December 2020 •

Published Online: 22 December 2020



H. Tang,<sup>1,a)</sup> B. K. Russell,<sup>1</sup> A. Maksimchuk,<sup>1</sup> P. T. Campbell,<sup>1</sup> M. J.-E. Manuel,<sup>2</sup> and L. Willingale<sup>1</sup>

## AFFILIATIONS

<sup>1</sup>Gerard Mourou Center for Ultrafast Optical Science, University of Michigan, 2200 Bonisteel Boulevard, Ann Arbor, Michigan 48109, USA

<sup>2</sup>General Atomics, San Diego, California 92121, USA

<sup>a)</sup>Author to whom correspondence should be addressed: [tanghm@umich.edu](mailto:tanghm@umich.edu)

## ABSTRACT

The spatial resolution and imaging characteristics of plastic scintillators are characterized using laser-driven proton beams. Laser-driven proton beams typically have broad energy spectra and are accompanied by relativistic electrons and high-energy photons, both potentially contributing to background noise. Different types and thicknesses of Eljen Technology scintillators are compared to determine their intrinsic point spread function. Point-projection imaging of a mesh is used to compare the imaging resolution of the scintillator to the usual imaging detector, radiochromic film, and is found to be reasonably comparable and sufficient for many experimental applications.

Published under license by AIP Publishing. <https://doi.org/10.1063/5.0022166>

## I. INTRODUCTION

Laser-driven proton radiography is a widely used technique to measure the time evolution of quasi-static electro-magnetic fields in high-energy-density physics (HEDP) experiments.<sup>1</sup> The proton source can be either a D<sup>3</sup>He implosion<sup>2</sup> or a target normal sheath acceleration (TNSA) driven proton beam.<sup>1,3</sup> The small effective source size and short emission times mean that the spatial and temporal resolution of the imaging can be very small (~10 μm for TNSA sources). Protons emitted from the source propagate to the main interaction of interest, where the local electromagnetic fields deflect the protons, altering the trajectories such that an image forms in the far-field detected proton profile.

The detectors typically used for imaging the proton beam are Californian resin 39 (CR39) or radiochromic film (RCF). These detectors are reliable: CR39 has absolute number calibration, RCF has good energy discrimination (due to the Bragg peak), and they both have excellent spatial resolution for imaging applications. However, CR39 and RCF are single use, request replacement between shots, need scanning to process and analyze data, and, in the case of CR39, require a time-consuming etching process. As proton radiography experiments move from being exclusively conducted at the high-energy glass-based laser systems, typically

having less than 10 shots per day, to new higher-repetition extremely high-power Ti:sapphire systems, CR39 and RCF are becoming less practical, leading to the implementation of scintillator-based detectors.<sup>4-7</sup> The luminescent yield (photons per incident proton) of the scintillator can be calibrated based on its thickness and manufactured structures, such as pixelation.<sup>8</sup> In addition to being multi-use, the scintillator is also expected to have a high spatial resolution, especially for experiments that need to resolve fine structures (<100 μm) over a relatively large area. For example, the measurement of the filamentation structures in the Weibel instability shows a structure with a size of 40 μm in a 6 × 6 mm<sup>2</sup> region;<sup>9</sup> the diagnostic of the surface wave in direct laser acceleration experiments requires to resolve a periodicity of 50 μm.<sup>10</sup>

Previous work has studied the intrinsic spatial resolution of monolithic organic scintillators using a monoenergetic proton source accelerated from a cyclotron proton source.<sup>7</sup> These results were promising for the use of thin scintillator detectors for the application of proton imaging. However, a laser-driven proton source has considerably different properties and operation conditions. The proton energy spectrum is typically broad and Maxwellian-like. When the proton reaches its Bragg peak in the detector material, which is the region of maximum energy loss in the proton stopping curve, the proton loses a large amount of kinetic energy in a very short

distance just before it stops, producing a large local radiation dose in the detector. Unless the detecting layer is very thin (as is the case for RCF), the proton energy range that will have Bragg peaks within the detecting layer can become significant. For proton radiography applications, the measurement of protons with a range of energies will lead to a reduction in the image quality: spatial smearing due to proton deflections being related to their velocities as given by the Lorentz force and by temporal smearing due to the protons having a range of transit times from the source to the interaction of interest. Furthermore, the laser-plasma interaction driving the proton source generates relativistic electrons and high-energy x rays that are a potential source of the background signal in the scintillators. Therefore, it is important to characterize the properties of the scintillators under these more complex conditions. One approach to distinguish and account for the contributions of the background electron signal is to use a mesh grid.<sup>5,6</sup> While this approach works for large scale structures such as the overall beam shape and dimensions, fine structures and imaging properties are lost.

Here, we characterize a variety of scintillator types and thicknesses using TNSA accelerated protons where a background of high-energy electrons and x rays is generated. The intrinsic point spread function (PSF) is measured using a proton beam and a resolution grid. The image resolution and contrast are also characterized and compared to RCF in a point-projection imaging setup using a micro-mesh.

## II. EXPERIMENTAL SETUP

The experiment was performed using the T-cubed laser at the University of Michigan. The laser pulses had a central wavelength of  $1.053 \mu\text{m}$  and energies of  $4.6 \pm 0.7 \text{ J}$  with a 400 fs full-width-at-half-maximum (FWHM) duration. An  $f/2$  off-axis parabolic mirror focused the p-polarized pulse onto a  $5 \mu\text{m}$  thick copper foil target at an incident angle of  $24^\circ$ . The elliptical focal spot had FWHM dimensions of  $3 \times 8 \mu\text{m}^2$ , giving a peak intensity of  $(4.3 \pm 0.9) \times 10^{19} \text{ W cm}^{-2}$ .

Figure 1 shows a schematic of the experimental setup. A Thomson Parabola Spectrometer (TPS) aligned along the rear target

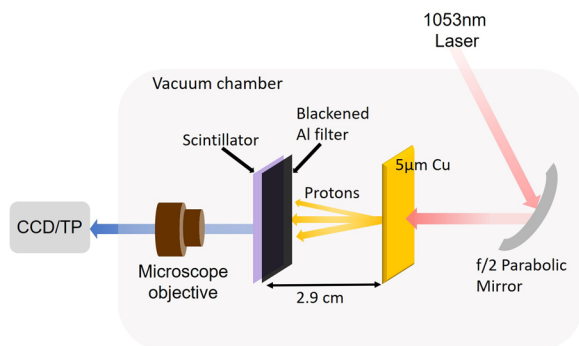


**FIG. 1.** A schematic of the experimental setup. A 1053 nm high intensity laser pulse is focused by a  $f/2$  parabolic mirror onto a  $5 \mu\text{m}$  Cu target to generate TNSA proton beams. The proton beam is measured either by the TP spectrometer to measure the energy spectrum or by the scintillator imaged onto a CCD with/without a microscope objective system to diagnose the spatial resolution.

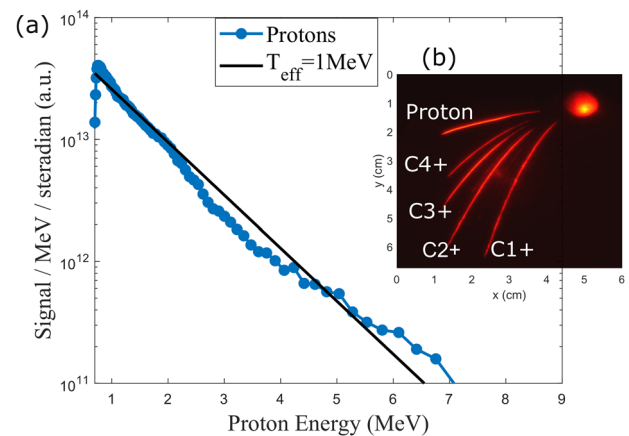


**FIG. 2.** (a) Proton energy spectrum. The blue dotted line is the experiment data, and the black solid line is the fitting line with a form of  $7 \times 10^{13} \cdot \exp(-e/T_{\text{eff}})$ , where  $T_{\text{eff}} = 1 \text{ MeV}$  is the effective proton energy. (b) Raw image of the Thomson parabola spectrometer. The top curve is the proton spectrum, and the curves below are the spectra for carbon ions.

normal direction was used to characterize the energy spectrum of the proton beam. In the TPS, accelerated protons and other ions pass through a pinhole and collimator to select a small solid angle before traveling through parallel electric and magnetic fields. Particles are deflected along certain trajectories in the electric and magnetic fields due to different charge to mass ratios and energies. The ions are then detected using a microchannel plate (MCP) coupled to a phosphor screen to produce an optical signal that can be imaged on a CCD camera. Each species forms a unique parabola on the detector screen shown in Fig. 2(b).

Once the proton beam had been characterized, a scintillator was placed along the proton beam path at 3 cm behind the target. Three different scintillator series from Eljen Technologies were investigated, EJ-228, EJ-212, and EJ-204.<sup>11</sup> These are thin, flexible, and readily available polyvinyltoluene-based scintillators that are easy to cut to a desired shape. Measurements were made using  $5 \times 5 \text{ cm}^2$  of the scintillating material with nominal manufacture thicknesses of  $100 \mu\text{m}$  and  $500 \mu\text{m}$  for the EJ-204 and EJ-212 series and  $50 \mu\text{m}$ ,  $100 \mu\text{m}$ , and  $500 \mu\text{m}$  for the EJ-228 series. Table I shows the actual measured thicknesses of each scintillator type, although we will refer to the scintillators by their manufactured thicknesses.

**TABLE I.** Scintillator thicknesses.

Scintillator type	Nominal thickness ( $\mu\text{m}$ )	Actual thickness ( $\mu\text{m}$ )
EJ-228	50	$49 \pm 3$
	100	$128 \pm 7$
	500	$359 \pm 3$
EJ-212	100	$113 \pm 9$
	500	$418 \pm 10$
EJ-204	100	$140 \pm 4$
	500	$483 \pm 4$

The scintillators were shielded from any stray laser light using  $50\ \mu\text{m}$  thick blackened aluminum foil placed in front of the scintillators, which was also used to create a shroud around the scintillators to reduce background light. When a proton beam passes through a scintillator, the kinetic energy is lost in the material, primarily to the electrons. Electrons are ionized or excited from the ground state to higher energy levels before a quick recombination or radiationless decay process ( $\sim\text{ps}$ ) accumulates them at a thermal equilibrium state. From this state, electrons de-excited to the ground level within  $\sim 2\ \text{ns}$  decay time and fluorescent light of wavelength at the range of  $370\ \text{nm}$ – $440\ \text{nm}$  are emitted. In our experiment, this emitted light was imaged onto a Coolsnap CF CCD for which the exposure time was much longer than the decay time.

Different imaging systems were used for the measurement of the point spread function (PSF), the relative signal contribution of electrons and x rays, and the ability to create point-projection images. To measure the PSF, a  $100\ \mu\text{m}$  thick tungsten resolution grid with knife edge slits (which stopped  $<6.8\ \text{MeV}$  protons) was placed in front of the Al foil filter and scintillator. To ensure the imaging system had a resolution better than the PSF of the scintillator, a Computar M1614-MP2 microscope objective collected the light emitted from the rear side of the scintillator, followed by a Computar M6Z1212-3S zoom lens mounted to the CCD that was placed outside the vacuum chamber. The averaged overall resolution of this system was  $15\ \mu\text{m}$  per pixel. The system resolution may fluctuate within a range of  $3\ \mu\text{m}$  per pixel because of the thickness variance of scintillators.

To determine the scintillator imaging capability, a transmission electron microscopy (TEM) mesh was placed  $1.7\ \text{mm}$  behind the proton source producing a magnified image of the mesh on the scintillator. The lower half of the scintillator was covered with RCF layers to create a direct comparison between the two detectors. A  $50\ \mu\text{m}$  thick Al filter still covered the target-facing side of the detector. The imaging system of this geometry only used a CCD attached with a zoom lens, and the spatial resolution was  $57\ \mu\text{m}$  per pixel.

### III. EXPERIMENTAL DATA

#### A. Proton beam spectrum and divergence

First, the proton spectrum in the target normal rear direction was characterized using the TPS. Figure 2(b) shows a raw TPS image with the uppermost parabola being the dispersed proton beam and the bright spot on the top right being the “straight-through” neutral spot, which acts as the reference for zero deflection. The additional parabolic signals, below the proton beam, are for different carbon ion species. The shot-to-shot proton energy spectrum variations for this experiment were primarily influenced by the parameters of laser energy and the positioning of the target surface with respect to the focal position. The maximum proton energy observed by the TPS on each shot was  $\sim 6.7\ \text{MeV}$  as shown in the spectrum in Fig. 2(a). A fit to the proton energy spectrum is shown as a black solid line with a form of  $7 \times 10^{13} \cdot \exp(-e/T_{\text{eff}})$ , with  $T_{\text{eff}} = 1\ \text{MeV}$  being the effective proton energy.

Figure 3 shows the whole proton image on the scintillator with rectangular aluminum filters of different thicknesses covering each quarter. The thicknesses of the four Al rectangles were  $12.5\ \mu\text{m}$ ,  $42.5\ \mu\text{m}$ ,  $82.5\ \mu\text{m}$ , and  $382.5\ \mu\text{m}$ ; correspondingly, they blocked

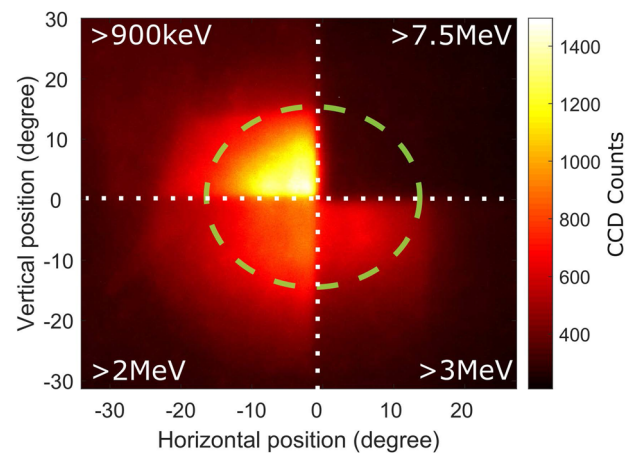


**FIG. 3.** Scintillator EJ-228 image with Al filters blocking protons with energies below  $900\ \text{keV}$ ,  $2\ \text{MeV}$ ,  $3\ \text{MeV}$ , and  $7.5\ \text{MeV}$ . The green dashed circle is the  $1/2$  peak intensity, corresponding to a  $15^\circ$  half-angle.

protons of energies below  $900\ \text{keV}$ ,  $2\ \text{MeV}$ ,  $3\ \text{MeV}$ , and  $7.5\ \text{MeV}$ . The intersection of the four rectangles was aligned to the center of the proton beam. The approximate extent of the proton beam on the scintillator is illustrated by the green dashed circle, which has a radius of  $0.8\ \text{cm}$ , corresponding to a half beam divergence of  $15^\circ$ .

As shown in Fig. 3, the top left region detecting protons above  $900\ \text{keV}$  had noticeably more signal than other three rectangles. As the filter thickness increased, a significant drop of signal is observed, as expected for a Maxwellian-like energy spectrum. In the top right region where the filter blocked all the protons, a negligibly low signal was detected. Since no proton contributes to the illumination in this region, the signal in this sector should only be the background due to electrons and x rays. Other studies have found that the scintillator signal due to high-energy electrons or x rays is insignificant compared to protons when using thin (sub-mm) scintillators.<sup>12–14</sup> Therefore, the signal generated by proton radiation dominates the emitted light, making proton imaging in this setup reliable.

#### B. Point spread function

To measure and calculate the intrinsic PSF for each scintillator, we attached a  $100\ \mu\text{m}$  thick tungsten resolution grid in front of each scintillator and the  $50\ \mu\text{m}$  Al filter. The grid consisted of several groups of slits with various widths. A calculation using SRIM<sup>16,17</sup> shows that a  $50\ \mu\text{m}$  Al filter would block electrons with energy  $<0.1\ \text{MeV}$ , carbon ions with energy  $<45\ \text{MeV}$ , and protons with energy  $<2.2\ \text{MeV}$ . Thus, the scintillator signal was only due to protons with energies in the range of  $2.2\ \text{MeV}$ – $6.7\ \text{MeV}$ , the high-energy cutoff. The protons propagated through the slits of the grid and the black aluminum foil before hitting the front side of each scintillator. The array of  $500\ \mu\text{m}$ -width slits was placed in front of the scintillator, with the center of the proton beam being aligned to the lowest edge of the slits, allowing the upper half of the proton beam to transmit and the lower half to be blocked.

Figure 4 shows the raw image of the  $50\ \mu\text{m}$  thick EJ-228 scintillator, where the circular edge is due to the objective aperture. The

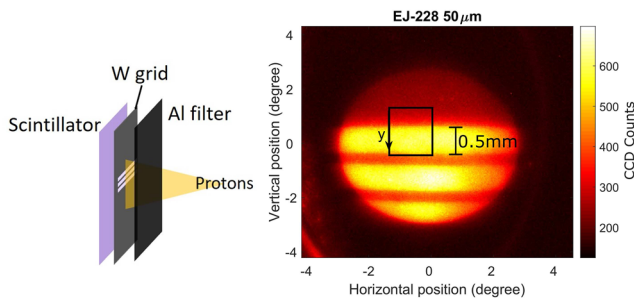


**FIG. 4.** Left: a schematic of the proton beam projection through the tungsten resolution slits on a  $50\ \mu\text{m}$  thick EJ-228 scintillator. The width of the slits (open region) is  $500\ \mu\text{m}$ , and the distance between the slits is  $215\ \mu\text{m}$ . The proton beam is centered at the lower edge of the slit group. Right: the scintillator image observed using a microscope objective limits the field of view to  $6^\circ$  and produces the circular edge to the image.

color scale is proportional to the light emission from the scintillator, i.e., the lighter regions are where the protons passed through the slit and the darker slots are the tungsten-blocked areas. Images of other scintillators looked very similar to Fig. 4 with only slightly magnification differences due to the scintillator thickness. To eliminate this error, we measured the magnification for every observation.

As protons propagate through the scintillator, energy is lost primarily to exciting electrons that subsequently emit optical photons. The primary (and then secondary) electrons that are formed are emitted with similar directionality and may go on to form further excited states and photon emission. The region of emission due to a single proton may therefore be blurred. This effect can be illustrated by the standard deviation,  $\sigma$ , of the PSF of the scintillating material. Lineouts across the upper edge of the first bright slot were taken along the direction of the arrow shown in Fig. 4. Since a microscope objective is used, the image is distorted to a small extent around the edge. Normalized intensities shown in Fig. 5 were calculated as the averaged intensity of the lineouts taken from the black rectangular area close to the central vertical axis of the objective field where the intensity distribution was comparatively uniform in the horizontal direction.

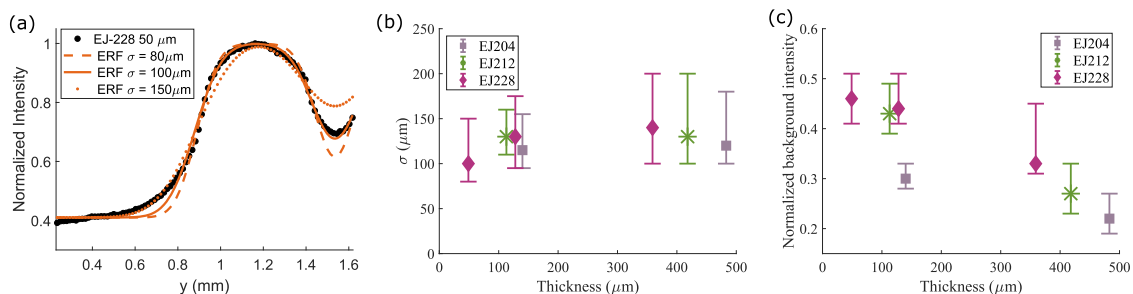
A compound Gauss error function (ERF) was employed to fit the experimental data and measure the point spread function given by the following equation:

$$\frac{A}{2} \left( 1 + \operatorname{erf} \left( \frac{x - \mu_1}{\sqrt{2}\sigma} \right) \right) - \frac{A}{2} \left( 1 + \operatorname{erf} \left( \frac{x - \mu_2}{\sqrt{2}\sigma} \right) \right) + C, \quad (1)$$

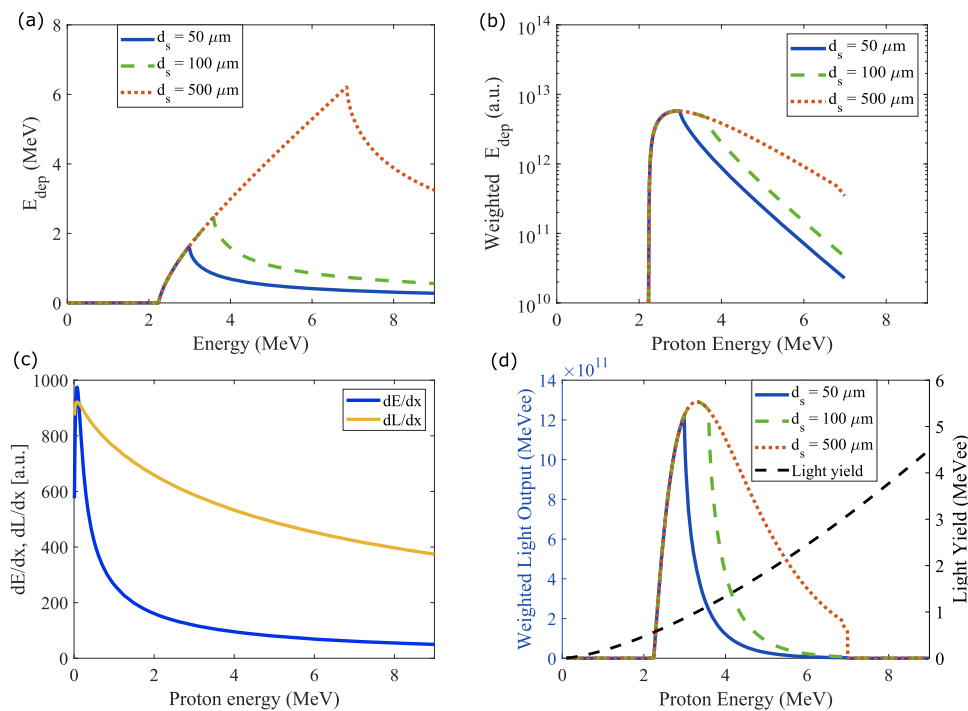
where  $A$  is the magnitude constant,  $\mu_1$  and  $\mu_2$  are the edge positions,  $\sigma$  is the standard deviation corresponding to the sigmoid scale of the curve, and  $C$  is a constant equal to  $(1 - A)$ .

Figure 5(a) shows the experimental data (black dots) along with ERF fitting curves (orange lines) for the  $50\ \mu\text{m}$  thick EJ-228 scintillator. The value of the standard deviation ranges from  $80\ \mu\text{m}$  to  $150\ \mu\text{m}$ . The maximum  $\sigma$  ( $150\ \mu\text{m}$ ) perfectly matches the foot region, while the minimum  $\sigma$  ( $80\ \mu\text{m}$ ) better matches the data peak. The standard deviation for other thicknesses and scintillator types is shown in Fig. 5(b).  $\sigma$  is taken for the best fit to the experimental curves, mainly among the normalized intensity value range of 20%–80%. For all scintillator types and thicknesses, there is not a strong dependence on thickness with  $\sigma$  values in the range of  $100\ \mu\text{m}$ – $130\ \mu\text{m}$ . The error bar is found by fitting to the 0%–20% normalized intensity to find the upper limit, and the 80%–100% normalized intensity to find the lower limit. For each scintillator type, the  $\sigma$  error bars are smaller for the thinner detector. Figure 5(c) shows a plot of the background signal normalized to peak intensity for each shot. Comparing the different scintillator types within similar thickness ranges, the background noise was generally largest for EJ-228, smaller for EJ-212, and smallest for EJ-204. Generally, the thicker scintillators for each type have lower background intensity, indicating a better image contrast. This is because the absolute CCD counts for the background, mainly due to high-energy electrons, are relatively flat, but the thicker scintillators generate more proton signal.

To understand the total light output from the scintillator, the weighting of the Maxwellian-like proton spectra needs to be considered. For this analysis, the proton energy spectra shift as it propagates through the  $50\ \mu\text{m}$  Al prior to the scintillator is accounted for, and protons with  $<2.2\ \text{MeV}$  are blocked. Figure 6(a) shows the deposited proton energy for a beam with a flat energy spectrum for scintillators with different nominal thicknesses. The protons with energies at  $3\ \text{MeV}$ ,  $3.6\ \text{MeV}$ , and  $6.8\ \text{MeV}$  deposit the maximum



**FIG. 5.** (a) Normalized intensity across the top proton bar of the  $50\ \mu\text{m}$  thick EJ-228 scintillator. The foot region (small  $y$  position) is the opaque tungsten area, and the intensity peak is where the proton passes through the open slit. The normalized intensity does not drop as much on the right due to the signal overlap from the second slit. The experimental data (black dots) are compared to ERF fitting curves with  $\sigma = 80\ \mu\text{m}$  (dotted line),  $100\ \mu\text{m}$  (solid), and  $150\ \mu\text{m}$  (dashed line). (b) Plot of the  $\sigma$  measurement vs scintillator thicknesses. (c) Plot of the background intensity normalized to the peak intensity of each shot vs scintillator thicknesses.



**FIG. 6.** How the proton energy deposition in scintillators and light yield varies for the different nominal scintillator thicknesses. (a) The deposited energy from protons with various energies, accounting for energy loss through the 50  $\mu\text{m}$  Al filter, into 50  $\mu\text{m}$  (blue solid line), 100  $\mu\text{m}$  (green dashed line), and 500  $\mu\text{m}$  (red dotted line) scintillators. (b) The energy deposition weighted by the exponential energy spectrum,  $dN/dE = 7 \times 10^{13} \cdot \exp(-eT_{\text{eff}})$ , with the 7 MeV cutoff energy. (c) The proton stopping power  $\frac{dE}{dx}$  and the scintillation light output per unit path length  $\frac{dL}{dx}$  as a function of proton energy. The dashed curves are the exponential weighted results. (d) The light yield as a response of full-stop proton energy (black dashed curve), which is the integral of the  $\frac{dL}{dx}$  [yellow solid curve in (c)] and energy spectrum weighted light yield  $L(E)$  in scintillators with certain thicknesses (blue, green, and red curves). The units are converted to equivalent electron energy (MeVee).

energy per proton for 50  $\mu\text{m}$ , 100  $\mu\text{m}$ , and 500  $\mu\text{m}$  scintillators, respectively. Higher energy protons do not reach the Bragg peak within the material, and so the total deposited energy decreases with proton energy. Using a proton beam with the exponential energy spectrum shown in Fig. 2, the energy deposition is modified by the fitting equation and an energy cutoff of 7 MeV is applied to estimate the weighted energy deposition, as shown in Fig. 6(b). The energy deposition is heavily weighted by the exponentially larger number of lower energy protons, meaning that the light yield is dominated by the low energy protons. For thicker scintillators, the range of proton energies that contribute significantly to the signal broadens slightly, but the energy at which the deposition peak occurs is constant.

The light output of the scintillator is a nonlinear response of the proton specific energy loss  $\frac{dE}{dx}$ . The light output follows Birks's law,  $\frac{dL}{dx} = S \frac{dE}{dx} \left[ 1 + k_B \left( \frac{dE}{dx} \right) \right]^{-1}$ , where  $\frac{dL}{dx}$  is the light output per unit path length,  $S$  is the scintillation efficiency, and  $k_B$  is an adjustable parameter for a particular material.<sup>15,18</sup> To estimate the light output,  $\frac{dL}{dx}$ , plotted in Fig. 6(c) (solid line), we take a typical value  $k_B \sim 0.01 \text{ g MeV}^{-1} \text{ cm}^{-2}$  and use SRIM stopping power tables for the scintillator. The exponential spectrum with  $T_{\text{eff}} = 1 \text{ MeV}$  sharpens the stopping power and weakens the response of high-energy protons. The light yield is estimated by integrating  $\frac{dL}{dx}$  over the distance for protons of various energies to completely stop and is plotted as the black dashed line in Fig. 6(d). Intuitively, the light yield per proton increases with proton energy. Figure 6(d) also plots the accumulated light output as a function of proton energy in scintillators with different thicknesses  $d_s$ , weighted to account for the Maxwellian-like energy spectra. Particles with  $< 4 \text{ MeV}$  contribute most to the light yield in 50  $\mu\text{m}$  and 100  $\mu\text{m}$  detectors (blue and green curves). Higher

energy protons have much less effect because they pass through the scintillator causing a sudden drop in light output. For the 500  $\mu\text{m}$  scintillator (red dotted curve), the light output comes from a larger range of proton energies. Therefore, the 500  $\mu\text{m}$  scintillator should have a higher absolute signal yield, and this is consistent with the relatively low normalized background intensity measured in Fig. 5(c). By taking the summation of the light yield over the whole proton energy range, the energy transfer efficiency from proton to light output is roughly 1.7%, 3.0%, and 5.5% for 50  $\mu\text{m}$ , 100  $\mu\text{m}$ , and 500  $\mu\text{m}$  scintillators, respectively. Unlike an accurate calculation,<sup>19</sup> this rough estimate ignores the proton spatial distribution and does not integrate over the whole solid angle and therefore likely overestimates the efficiency.

### C. Effective spatial resolution and contrast

The 100  $\mu\text{m}$  EJ-204 scintillator was compared with RCF to investigate the imaging capabilities of each detector. The lower half of the scintillator was covered by two layers of RCF, and a third layer of RCF was placed behind to capture any protons that pass through the scintillator. The three RCF layers measured protons with energies of  $2.4 \pm 0.16 \text{ MeV}$ ,  $4.0 \pm 0.11 \text{ MeV}$ , and  $6.3 \pm 0.07 \text{ MeV}$ , respectively. Note that the RCF contains a very thin active layer in the range of 8  $\mu\text{m}$ –12  $\mu\text{m}$ , meaning that a particular RCF layer is sensitive to a very narrow energy range ( $\sim 0.2 \text{ MeV}$ ). This contrasts with the relative broad energy range the scintillators are sensitive to (see Fig. 6). In this calculation, we used the actual thickness (140  $\mu\text{m}$ ) for the scintillator. A TEM mesh, with a pitch of 62  $\mu\text{m}$  (a hole width of 37  $\mu\text{m}$  and a bar width of 25  $\mu\text{m}$ ), was placed 1.7 mm behind the proton source was projected onto the detectors. The RCF was

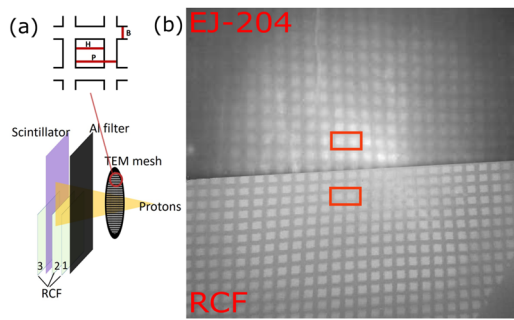


**FIG. 7.** (a) The sketch of TEM mesh and pixel sizes,  $P = 62 \mu\text{m}$ ,  $H = 37 \mu\text{m}$ , and  $B = 25 \mu\text{m}$ . (b) The TEM imprint on the proton beam as observed by the EJ-204 scintillator (top) and RCF (bottom).

then scanned and compared to the scintillator result, as shown in Fig. 7. Using the dose to optical-density (OD) conversion equation obtained by Bin *et al.*,<sup>20</sup>  $\text{dose} = 374.6 \cdot \text{OD} + 2557 \cdot \text{OD}^{3.085}$ , and parameters of the scanner consisting of a square pixel size of  $40 \mu\text{m}$  and a resolution of 600 dpi, a maximum proton number per pixel  $\sim 1.2 \times 10^8$  and a total proton number  $\sim 1.9 \times 10^{12}$  detected on the RCF were roughly calculated.

Both detectors imaged the TEM grid with a magnification of 16. The mesh projected onto the RCF has a sharper edge and higher resolution than the scintillator. To quantify the spatial resolution of the RCF and scintillator, lineouts were taken across two pitches of the mesh from a symmetric position across the splicing line. Since the scale of the two pitches is too small to provide enough data showing the continuous intensity change near the grid edge, and the grid edges are tilted at a tiny angle, an oversampling method is used to construct oversampled lineouts. The normalized value of each pixel of the image is used as the “intensity.” The pixel positions were then

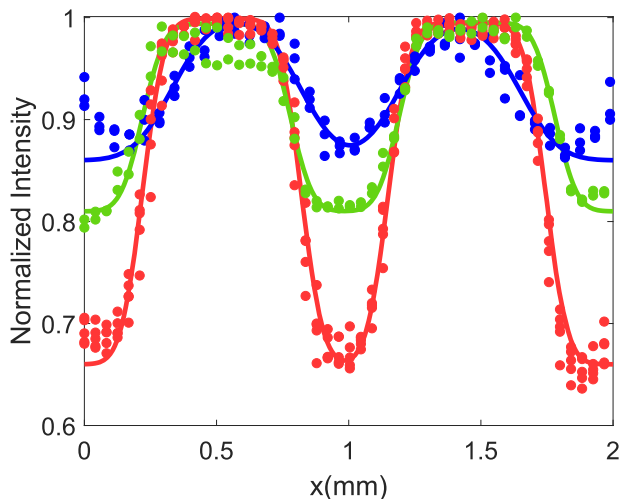


**FIG. 8.** Oversampled lineouts across two pitches in the images of the first RCF layer (red), the second RCF layer (green), and the scintillator (blue). The solid lines are the edge response curve fits.

projected onto a line perpendicular to the grid edge, which was taken as the measurement axis. We repeated this process for a group of consecutive rows to get the dotted lines shown in Fig. 8. ERF fitting curves with standard deviations of  $65 \mu\text{m}$  and  $115 \mu\text{m}$  were used as the edge response, which is also called the edge spread function (ESF) for the RCF (red solid line for the first layer and green for the second layer) and scintillator (blue solid line). The edge response is the system response to a sharp straight discontinuity, which is the detector response of a knife edge illuminated by the proton beam in our experiment.<sup>21</sup>

The fitting curves were applied for two analyses. One was to calculate the image contrast based on the Michelson contrast formula,

$$\text{Contrast} = \frac{I_{\text{max}} - I_{\text{min}}}{I_{\text{max}} + I_{\text{min}}}. \quad (2)$$

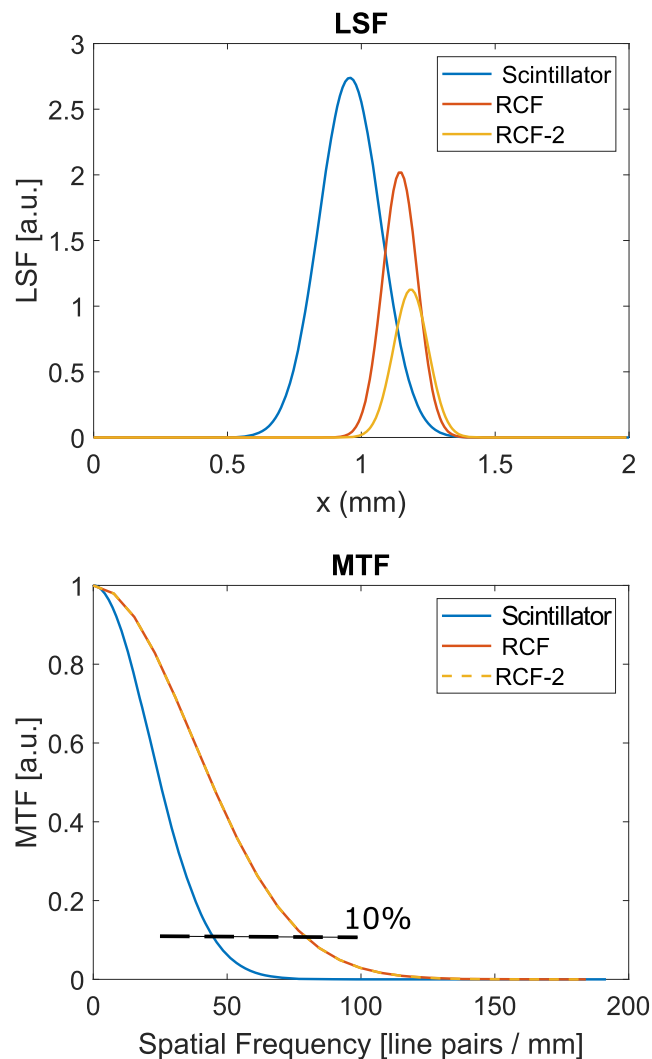


**FIG. 9.** The line spread function (top) and the modulation transfer function (bottom). The resolution of the scintillator was around  $26 \mu\text{m}$  and  $9 \mu\text{m}$  for the RCF.

The image contrasts are  $0.22 \pm 0.04$ ,  $0.13 \pm 0.05$ , and  $0.073 \pm 0.02$  for the first RCF layer, second RCF layer, and scintillator, respectively. While it might be expected for the first RCF layer to be more affected by the background signal, the large number of low energy protons (2.1 MeV–2.7 MeV) mean that the contrast is best. For all three scintillator series, the contrast of the thicker scintillator (500  $\mu\text{m}$ ) is larger than those of the thinner ones (50  $\mu\text{m}$ , 100  $\mu\text{m}$ ) due to the longer potential propagation distance providing more opportunities for protons or the generated electrons to scatter creating a broader region of emission.<sup>7</sup>

The second calculation was to derive the resolution limit of the scintillator following the steps in Refs. 22 and 23. The derivative of the edge response is taken to obtain the line spread function (LSF), shown in Fig. 9. Then, the modulation transfer function (MTF) is calculated by taking the Fourier transform of the LSF and normalized to its value at zero frequency in Fig. 9. The first zero point of the MTF represents the reciprocal of the effective resolution of the detector. However, since the first zero point on the MTF curves is difficult to identify and it corresponds to 0 contrast, here, we define the resolution using the 10% MTF value above which the MTF curves look similar for different edge responses even though it is not from an ERF fitting curves.<sup>21</sup> From the blue curve in Fig. 9 (bottom), the intrinsic resolution of the scintillator is  $\sim 22 \mu\text{m}$ . Both two RCF sheets (red and yellow curves) have a same resolution of  $\sim 12 \mu\text{m}$ .

There are several reasons that are likely to degrade the imaging quality of the scintillator, primarily due to the thickness of the “active” region. Protons will randomly scatter, changing the direction of the proton, as energy is lost to the material. Additionally, the generated electron cloud from the ionization caused by stopping the proton will form a diffuse optical emission. This differs from RCF, where the active detection layer is very thin along the propagation direction of the proton such that the scattering and blurring effects are minimized.

#### IV. SUMMARY

In conclusion, a 4.6 J, 400 fs pulse laser focused onto a 5  $\mu\text{m}$  thick Cu foil generated protons with a virtual source size of  $\sim 10 \mu\text{m}$ ,  $30^\circ$  divergence, and maximum energy up to 6.7 MeV. The laser accelerated proton beam was utilized to measure the spatial resolution of EJ-204, EJ-212, and EJ-228 scintillators with different thicknesses and was compared to RCF. The standard PSF for the scintillators ranges from 100  $\mu\text{m}$  to 130  $\mu\text{m}$ . The thicker scintillator detectors achieved better imaging contrast. In an imaging geometry, the effective resolution limit for the scintillator was around 22  $\mu\text{m}$ , determining scintillators to be a feasible substitute for RCF in many situations. With a sufficient high resolution and multi-use features, the scintillators characterized are a flexible beam profile detector for laser-driven proton diagnosis and radiography applications.

#### ACKNOWLEDGMENTS

This work was supported by internal research and development funds at General Atomics and was supported by DOE Office of Science, Fusion Energy Sciences under Contract No. DE-SC0019076: the LaserNetUS initiative at the University of Michigan. B.K.R. was

supported by the National Science Foundation under Grant No. 1751462.

#### DATA AVAILABILITY

The raw data were generated on the T-cubed laser at the Gerard Mourou Center for Ultrafast Optical Science at the University of Michigan. The data that support the findings of this study are available from the corresponding author upon reasonable request.

#### REFERENCES

- 1 M. Borghesi, A. J. Mackinnon, D. H. Campbell, D. G. Hicks, S. Kar, P. K. Patel, D. Price, L. Romagnani, A. Schiavi, and O. Willi, “Multi-MeV proton source investigations in ultraintense laser-foil interactions,” *Phys. Rev. Lett.* **92**, 055003 (2004).
- 2 C. K. Li, F. H. Séguin, J. A. Frenje, J. R. Rygg, and R. D. Petrasso, “Monoenergetic proton backlighter for measuring E and B fields and for radiographing implosions and high-energy density plasmas,” *Rev. Sci. Instrum.* **77**, 10E725 (2006).
- 3 S. P. Hatchett, C. G. Brown, T. E. Cowan, E. A. Henry, J. S. Johnson, M. H. Key, J. A. Koch, A. B. Langdon, B. F. Lasinski, R. W. Lee, A. J. Mackinnon, D. M. Pennington, M. D. Perry, T. W. Phillips, M. Roth, T. C. Sangster, M. S. Singh, R. A. Snavely, M. A. Stoyer, S. C. Wilks, and K. Yasuike, “Electron, photon, and ion beams from the relativistic interaction of petawatt laser pulses with solid targets,” *Phys. Plasmas* **7**, 2076 (2000).
- 4 J. S. Green, D. C. Carroll, C. Brenner, B. Dromey, P. S. Foster, S. Kar, Y. T. Li, K. Markey, P. McKenna, D. Neely, A. P. L. Robinson, M. J. V. Streeter, M. Tolley, C.-G. Wahlström, M. H. Xu, and M. Zepf, “Enhanced proton flux in the MeV range by defocused laser irradiation,” *New J. Phys.* **12**, 085012 (2010).
- 5 B. Aurand, L. Senje, K. Svensson, M. Hansson, A. Higginson, A. Gonoskov, M. Marklund, A. Persson, O. Lundh, D. Neely, P. McKenna, and C.-G. Wahlström, “Manipulation of the spatial distribution of laser-accelerated proton beams by varying the laser intensity distribution,” *Phys. Plasmas* **23**, 023113 (2016).
- 6 L. Senje, “Detector development, source characterization and novel applications of laser ion acceleration,” *Ph.D. thesis* (Lund University, 2017).
- 7 M. J.-E. Manuel, J. Strehlow, J. S. Green, D. Parker, E. L. Alfonso, J. Jaquez, L. Carlson, D. Neely, F. N. Beg, and T. Ma, “Intrinsic resolution limits of monolithic organic scintillators for use in rep-rated proton imaging,” *Nucl. Instrum. Methods Phys. Res., Sect. A* **913**, 103 (2019).
- 8 M. J.-E. Manuel, H. Tang, B. Russell, L. Willingale, A. Maksimchuk, J. S. Green, E. L. Alfonso, J. Jaquez, L. Carlson, D. Neely, and T. Ma, “Enhanced spatial resolution of thin inorganic scintillators for use in rep-rated imaging and spectroscopy applications,” *Rev. Sci. Instrum.* **91**, 103301 (2020).
- 9 K. Quinn, L. Romagnani, B. Ramakrishna, G. Sarri, M. E. Dieckmann, P. A. Wilson, J. Fuchs, L. Lancia, A. Pipahl, T. Toncian, O. Willi, R. J. Clarke, M. Notley, A. Macchi, and M. Borghesi, “Weibel-induced filamentation during an ultrafast laser-driven plasma expansion,” *Phys. Rev. Lett.* **108**, 135001 (2012).
- 10 L. Willingale, A. G. R. Thomas, P. M. Nilson, H. Chen, J. Cobble, R. S. Craxton, A. Maksimchuk, P. A. Norreys, T. C. Sangster, R. H. H. Scott, C. Stoeckl, C. Zuleck, and K. Krushelnick, “Surface waves and electron acceleration from high-power, kilojoule-class laser interactions with underdense plasma,” *New J. Phys.* **15**, 025023 (2013).
- 11 Eljen Technology, <https://eljentechnology.com/products>, 2020.
- 12 L. Chen, X. Ouyang, B. Liu, J. Liu, L. Quan *et al.*, “Compensational scintillation detector with a flat energy response for flash X-ray measurements,” *Rev. Sci. Instrum.* **84**, 013103 (2013).
- 13 A. Kumar, “An experimental study of the relative response of plastic scintillators to photons and beta particles within the context of tritium,” M.S. thesis (UOIT, 2011).
- 14 J. S. Green, M. Borghesi, C. M. Brenner, D. C. Carroll, N. P. Dover, P. S. Foster, P. Gallegos, S. Green, D. Kirby, K. J. Kirkby, P. McKenna, M. J. Merchant, Z. Najmudin, C. A. J. Palmer, D. Parker, R. Prasad, K. E. Quinn, P. P.

Rajeev, M. P. Read, L. Romagnani, J. Schreiber, M. J. V. Streeter, O. Tresca, C.-G. Wahlström, M. Zepf, and D. Neely, "Scintillator-based ion beam profiler for diagnosing laser-accelerated ion beams," *Proc. SPIE* **8079**, 807919 (2011).

<sup>15</sup>G. V. O'Rielly, N. R. Kolb, and R. E. Pywell Saskatchewan, "The response of plastic scintillator to protons and deuterons," *Nucl. Instrum. Methods Phys. Res., Sect. A* **368**, 745–749 (1996).

<sup>16</sup>J. F. Ziegler, M. D. Ziegler, and J. P. Biersack, "SRIM—The stopping and range of ions in matter (2010)," *Nucl. Instrum. Methods Phys. Res., Sect. B* **268**, 1818–1823 (2010).

<sup>17</sup>M. J. Berger, J. S. Coursey, and M. A. Zucker, ESTAR, PSTAR, and ASTAR: computer programs for calculating stopping-power and range tables for electrons, protons, and helium ions (version 1.21), <http://physics.nist.gov/Star>, 1999.

<sup>18</sup>J. B. Birks, *The Theory and Practice of Scintillation Counting* (Macmillan, New York, 1964).

<sup>19</sup>D. A. Oraini, *Sci. Technol. Nucl. Install.* **2018** 6432380.

<sup>20</sup>J. H. Bin, Q. Ji, P. A. Seidl, D. Raftrey, S. Steinke, A. Persaud, K. Nakamura, A. Gonsalves, W. P. Leemans, and T. Schenkel, "Absolute calibration of GafChromic film for very high flux laser driven ion beams," *Rev. Sci. Instrum.* **90**, 053301 (2019).

<sup>21</sup>S. W. Smith, *The Scientist and Engineer's Guide to Digital Signal Processing*, 1st ed. (California Technical Publishing, 1997), pp. 426–428.

<sup>22</sup>S. Najafi and K. Madanipour, "Measurement of the modulation transfer function of a charge-coupled device array by the combination of the self-imaging effect and slanted edge method," *Appl. Opt.* **52**, 4724 (2013).

<sup>23</sup>U. Neitzel, E. Buhr, G. Hilgers, and P. R. Granfors, "Determination of the modulation transfer function using the edge method: Influence of scattered radiation: Scatter influence on MTF determination," *Med. Phys.* **31**(12), 3485–3491 (2004).